Nano and micro $U_{1-x}Th_xO_2$ solid solutions: From powders to pellets

Luca Balice [a, b], Daniel Bouëxière [a], Marco Cologna [a], Andrea Cambriani [a], Jean-François Vigier [a], Emanuele De Bona [a], Gian Domenico Sorarù [b], Christian Kübel [c], Olaf Walter [a, *], Karin Popa [a, **]

[a] European Commission, Joint Research Centre, Nuclear Safety and Security Directorate, P.O. Box 2340, Karlsruhe, Germany
[b] Dipartimento di Ingegneria Industriale, Università di Trento, Via Sommarive 9, 38123 Trento, Italy
[c] Institute of Nanotechnology & Karlsruhe Nano Micro Facility, Karlsruhe Institute of Technology, P.O. Box 3640, Karlsruhe, Germany

HIGHLIGHTS

- First report on the hydrothermal synthesis of $U_{1-x}Th_xO_2$ nanocrystals through hydrothermal decomposition of oxalates.
- Facile to perform reproducible synthesis of nanosized mixed oxides.
- Access to homogeneous, highly sinterable powders.
- No grain size effect observed on the hardness or elastic modulus.
- Serving as models for high burn-up structures in spent fuel.

GRAPHICAL ABSTRACT
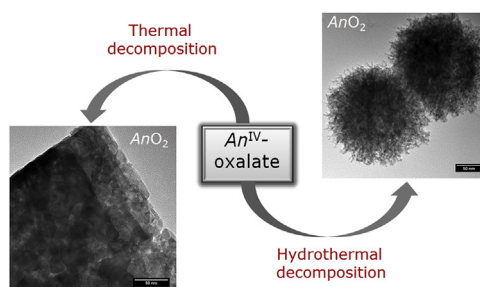
ABSTRACT

Nuclear fuels production, structural materials, separation techniques, and waste management, all may benefit from an extensive knowledge in the nano-nuclear technology. In this line, we present here the production of $U_{1-x}Th_xO_2$ ($x = 0$ to 1) mixed oxides nanocrystals (NC's) through the hydrothermal decomposition of the oxalates in hot compressed water at 250 °C. Particles of spherical shape and size of about 5.5–6 nm are obtained during the hydrothermal decomposition process. The powdery nanocrystalline products were consolidated by spark plasma sintering into homogeneous mixed oxides pellets with grain sizes in the 0.4 to 5.5 μm range. Grain growth and mechanical properties were studied as a function of composition and size. No grain size effect was observed on the hardness or elastic modulus.
© 2017 The Authors. Published by Elsevier B.V. This is an open access article under the CC BY license (http://creativecommons.org/licenses/by/4.0/).

1. Introduction

The thorium-uranium fuel cycle has some intriguing capabilities over the traditional one [1]. Besides the higher content as resource, fertile [232]Th has other advantages compared to uranium. From the physicochemical point of view, thorium has only one naturally occurring isotope ([232]Th) and one stable oxidation state (4+). Thoria (ThO_2) presents higher melting point and thermal conductivity compared to UO_2, as well as lower thermal expansion coefficient, positive properties for possible application as a nuclear fuel. In addition, the thorium fuel cycle would produce much lower quantities of transuranic elements, reducing the radiotoxicity of the waste and preventing proliferation of irradiated thorium-based

fuel, presenting superior plutonium burning in Th-based mixed oxides (MOX) [1,2]. Thus, thorium can be potentially employed in any type of nuclear reactor. However, in the near future the most interesting solution would be its integration in the currently operating thermal light water reactors as Th-based MOX [3]. Some experience is already available from the past [4]. Nevertheless much effort still has to be done to judge all the advantages and drawbacks of thorium fuel cycle.

One aspect of paramount importance is the assessment of the grain size dependent properties of the fuel. It is well known that the microstructure of dense oxides fuels with an initial grain size of several micrometres, when irradiated at high burnups and low temperatures, show areas with a porous sub-micrometre-grained microstructure, often called the "high burnup structure" (HBS) [5].

One of the challenges of achieving high density Th-based MOX stems from the very high melting point of ThO_2 which leads to high sintering temperatures. A possible solution to this issue consists in the reduction of the particle size of the powder down to nanometric scale [6–8]. UO_2 and ThO_2 powders have already been produced using mild methods, such as the thermal decomposition of the actinide oxalates using appropriate annealing conditions (above 600 °C) [9]. However, the sintering behaviour of the powders was not optimal, due to the presence of platelet-shaped agglomerates [10].

We have recently optimised this process by applying hydrothermal decomposition of An^{IV}-oxalates at much lower temperature [11]. This new approach proved to be a clean, flexible and powerful way to produce highly reactive nanocrystalline ThO_2, UO_2 and PuO_2 of spherical shape (Fig. 1).

The size and shape of the crystals, together with their increased reactivity, enables the one-step consolidation of homogeneous nanostructured MOX allowing separate effect studies on the properties of fuels for advanced reactors. We have extended this approach towards (U,Th)-MOX and here we present the first low-temperature synthesis (250 °C) of the $U_{1-x}Th_xO_2$ ($x = 0$ to 1) solid solutions. The powders were consolidated by Spark Plasma Sintering (SPS) at different temperatures in order to create a range of grain sizes and to study the influence of the composition and microstructure on the mechanical properties by nanoindentation.

2. Materials and methods

2.1. Synthesis and material processing

2.1.1. Synthesis of the $U_{1-x}Th_xO_2$ NC's by hydrothermal decomposition of the oxalates

This synthesis route consists of the hydrothermal decomposition of oxalates at low temperature [11]. The decomposition occurred in an autoclave made of two layers, the inner piece was a Teflon container and the external part is a stainless steel cylinder tightly screwed. Compared to classical oxalates decomposition by calcination, this method employed not only temperature, but also pressure to achieve the conversion into oxide. Indeed, a small amount of water was added to the powder and the obtained solution is mixed by stirring. Hence, inside the autoclave the increasing temperature caused the evolution of water and gases which raised the pressure in the autoclave.

Solutions of U^{IV} (0.5 M, obtained by electroreduction of $UO_2(NO_3)_2$ solution in 4 M HNO_3 containing 0.5 M of hydrazine) and Th^{IV} (1.9 M in 8 M HNO_3) were mixed in given proportions (U:Th = 100:0; 85:15; 70:30; 59:41; 50:50; 40:60; 22:78; 0:100 *mol* %). Then a concurrent coprecipitation [12,13] was induced by adding a stoichiometric amount of 1 M solution of oxalic acid. The resulting precipitate was washed with water and dried under vacuum overnight. Afterwards, working under argon, the autoclave

was filled with about 100 mg (mixed)-oxalate powder, 3 ml water and a small amount of hydrazine (20-50 μl in order to prevent oxidation of U^{IV}) and the reaction was performed for 18 h at 250 °C under continuous stirring. The resulting $U_{1-x}Th_xO_2$ NC's were washed with water, ethanol and acetone, in order to gradually decrease the polarity of the solution.

For pure ThO_2 no hydrazine or argon was required. In the case of the uranium-rich phases it turned out that it is of real advantage to work under oxygen free conditions as otherwise oxidation of the U^{IV} to $UO_2(OH)_2$ or U_4O_9 might proceed. Furthermore, in order to control the size of the $U_{1-x}Th_xO_2$ NC's, it is essential to work in a non-oxidising environment.

2.1.2. Spark plasma sintering

Two compositions were selected for sintering in SPS: $U_{0.50}Th_{0.50}O_2$ and $U_{0.85}Th_{0.15}O_2$. Sintering was performed with a SPS (FCT, Germany) installed in a glove-box flushed with argon gas [14]. Approximately 300 mg of powder were loaded in graphite dies and pre-compacted with 6 mm diameter graphite punches at 18 MPa. A graphite separation paper was wrapped around the sample in order to facilitate the extraction of the sintered material from the die. The pressure was raised from 18 to 68 MPa in 1 min at room temperature. The samples were sintered in vacuum at different maximum temperatures (from 1300, 1540 and 1700 °C), with a dwell time of 2 min, a heating and cooling rate of 200 °C/min. The constant pressure of 68 MPa was kept during the whole thermal treatment. The relative density of the samples during sintering are derived from the displacement of the piston during heating, after correcting for thermal and elastic strains of the sample and the system, by subtracting the cooling curve. The following equation was used to calculate the relative density as a function of the temperature ρ(T):

$$\rho(T) = \frac{\rho_f h_f}{h_f + s_f - s(T)}$$

where s(T) is the temperature dependent displacement after correction, s_f the total displacement after correction, ρ_f and h_f the final density and height of the sintered samples, respectively.

2.2. Physicochemical characterisation

2.2.1. XRD analysis

Room-temperature XRD analyses were performed on a Rigaku Miniflex 600 diffractometer. The particle sizes of the $U_{1-x}Th_xO_2$ NC's was calculated from the XRD data using the Scherrer equation based each on the full width at half maximum for six selected peaks in the 2θ range between 25 and 80°.

The thermal behaviour was investigated by high temperature X-ray diffraction. The data were collected on a Bruker D8 X-ray diffractometer mounted with a curved Ge (1,1,1) monochromator, a copper ceramic X-ray tube (40 kV, 40 mA), a LinxEye position sensitive detector and equipped with an Anton Paar HTK 2000 chamber. Measurements were conducted up to 1000 °C under helium, in the angle range $16° \leq 2\theta \leq 90°$ with a 2θ step size of 0.017°.

2.2.2. Microscopic characterisation

Transmission electron microscopy (TEM) studies were performed using an aberration (image) corrected FEI Titan 80-300 operated at 300 kV providing a nominal information limit of 0.8 Å in TEM mode and a resolution of 1.4 Å in STEM mode. TEM images have been recorded using a Gatan US1000 slowscan CCD camera, STEM images have been recorded using a Fischione high-angle annular dark-field (HAADF) detector with a camera length of
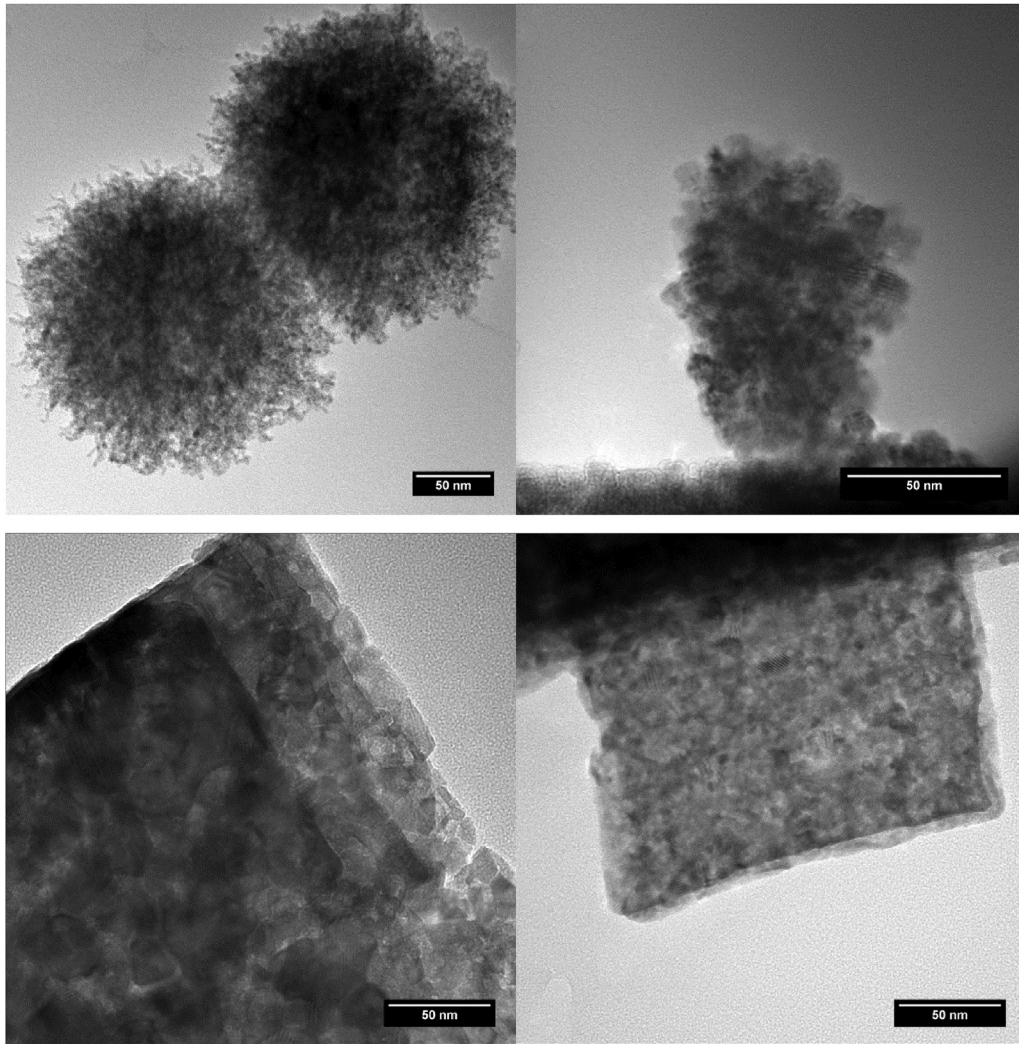
Fig. 1. Transmission electron micrographs of nanocrystalline UO₂ (left) and ThO₂ (right) obtained by hydrothermal (up) and thermal (down) [9] oxalate decomposition processes.

195 mm. The samples for analysis have been prepared on carbon coated copper grids by dropping coating with a suspension of the nanoparticles in ethanol.

Scanning electron microscopy (SEM) images were recorded with a Tescan Vega microscope. The line intercept method without correction factor was used to estimate the average grain size either on polished and thermally etched surfaces or on fracture surfaces. Thermal etching was performed for 30 min at a temperature 150 °C lower than the maximal sintering temperature. For the samples sintered at the lowest temperature (1300 °C), thermal etching was not effective and thus the grain size was measured on fracture surfaces, being the fracture for those samples intragranular.

2.2.3. Nanoindentation and hardness measurements

Nanoindentation measurements were carried out in order to measure Young's modulus (E) and nanoindentation hardness (H_{IT}) on mirror polished samples. Load-displacement curves were acquired with an IBIS nano-indenter (Fischer-Cripps Laboratories Pty Ltd.) equipped with a diamond Berkovich indenter (3-sided pyramid). Instrument's noise floor resolution for load and displacement are 70 nN and 0.1 nm respectively. For each sample 4 different maximum loads (50, 80, 110 and 150 mN) were applied with at least 15 indentations for each load.

Data analysis was carried out according to the Oliver-Pharr method [15]. Prior to every indentation run a check on a fused silica standard was performed. After indentation the residual impressions were imaged with SEM in order to assess the presence of cracking, delamination, piling up (flow of material around the edge of the indentation) or excessive sink-in, which would affect the validity of the Oliver-Pharr analysis.

3. Results and discussions

3.1. Powder synthesis

The hydrothermal decomposition of the $(U_{1-x}Th_x)$-oxalates formed by coprecipitation resulted in pure $U_{1-x}Th_xO_2$ NC's, as proved by XRD (Fig. 2a). From the XRD analysis, the lattice parameter and the crystallite size were measured as function of composition (Fig. 2b).

The lattice parameters for the present nanocrystalline $U_{1-x}Th_xO_2$ solid solutions agree quite well with the results of Trzebiatovski and Selwood (1950) [16] in the uranium-rich region, with the noticeable deviation from the Vegard's law reported for calcined samples [17,18]. The intercept of the linear fit for UO₂ of the present data is 5.447 Å, possibly via partial oxidation of U^{IV} to higher oxidation state(s) under air atmosphere. The relatively fast oxidation of uranium-rich compositions is in agreement with the high
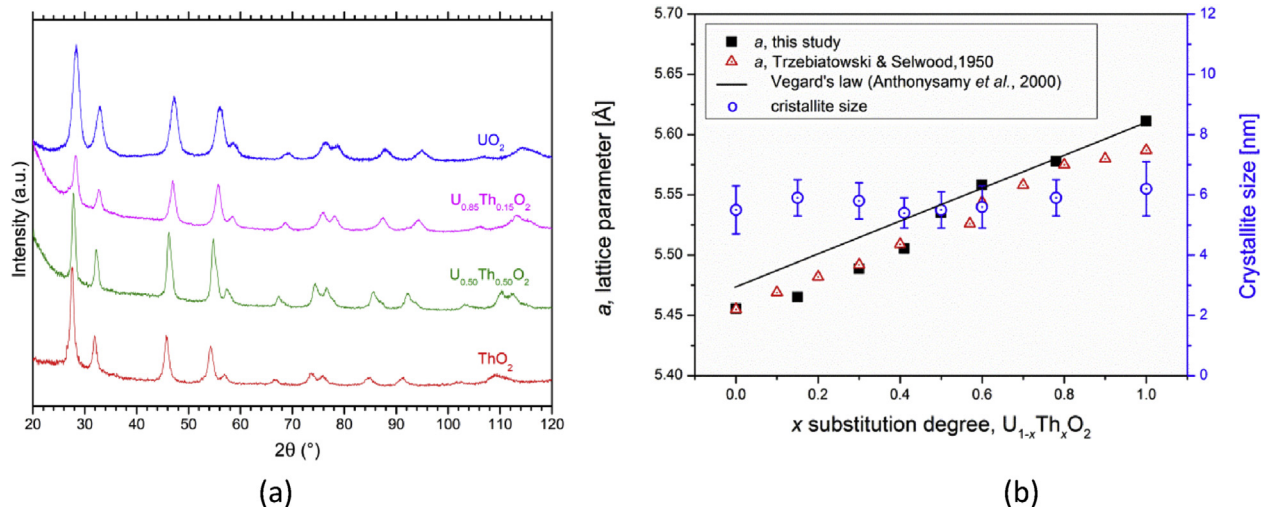
Fig. 2. (a) XRD patterns of two selected nanocrystalline $U_{1-x}Th_xO_2$ solid solutions obtained by hydrothermal decomposition of the corresponding oxalates. (b) Variation of the lattice parameter and the crystallite size as a function of the substitution degree x in the $U_{1-x}Th_xO_2$ solid solutions.

reactivity of the nanopowder reported here. It is interesting to note that the lattice parameter of the thorium-rich compositions ($x \geq 0.5$) agree very well with the Vegard's law reported for thermally-treated samples, suggesting (*i*) the stabilising effect of thorium for the 4 + oxidation state of uranium [19] and (*ii*) the absence of any observable size effect on the lattice parameters for pure ThO_2 and $U_{1-x}Th_xO_2$ MOX nanoparticles ($x \geq 0.5$), at least down to a size of about 6 nm. Fig. 2b also indicates that the crystallite size of the $U_{1-x}Th_xO_2$ solid solutions is constant around 5.5−6 nm, independent of the chemical composition.

The crystallite size calculated from the XRD data fits to the primary particle size seen by TEM, as shown in Fig. 3 for the $U_{0.85}Th_{0.15}O_2$ and $U_{0.50}Th_{0.50}O_2$ compositions. Moreover, the TEM analyse shows that the nanocrystals produced during hydrothermal decomposition of the oxalates have agglomerated to form aggregates with a diameter of about 100−200 nm. The agglomerates formed here do not show the plate-like morphology characteristic for the pseudomorphic thermal conversion of the oxalate. This might be due to stirring during the reaction or an effect of the changed reaction mechanism proceeding in water at temperatures of ca 250 °C compared to the solid state decomposition at a temperature higher than 600 °C.

3.2. Grain growth of $U_{1-x}Th_xO_2$ NC's

The growth of the $U_{1-x}Th_xO_2$ crystallites was investigated by high temperature X-ray diffraction of the $U_{0.85}Th_{0.15}O_2$ and $U_{0.50}Th_{0.50}O_2$ compositions (Fig. 4). Depending on the temperature one can see that the particles grow with increasing temperature: the pure UO_2 shows the highest increase in particle size from below 6 to over 100 nm, followed by $U_{0.85}Th_{0.15}O_2$. For $U_{0.5}Th_{0.5}O_2$ an increase to about 80 nm is observed at 1000 °C whereas ThO_2 remains nearby unchanged at this temperature with the particles being still smaller than 10 nm.

The very limited crystal growth of ThO_2 below 1000 °C compare to UO_2 [20,21] is in agreement with the lower diffusion of this element in its oxides which is reflected in the higher melting point and sintering temperature of ThO_2 compared to UO_2. The mixed oxides $U_{0.85}Th_{0.15}O_2$ and $U_{0.50}Th_{0.50}O_2$ exhibit an intermediate behaviour compared to the pure end members. Similar behaviour was observed in the case of $Th_{1-x}Ce_xO_2$ solid solutions [22], with a domain corresponding to the elimination of the crystal defects

below 700-800 °C and one typical to the crystallite growth above this temperature.

3.3. Sintering behaviour

The densification curve for $U_{0.50}Th_{0.50}O_2$ and $U_{0.85}Th_{0.15}O_2$ up to 1700 °C is reported in Fig. 5 showing the relative density (observed density/theoretical density) as a function of temperature. The very first part of the curve at room temperature is the densification due to the increase of the pressure from 18 to 68 MPa. Both powder start from a low relative density below 0.4. Upon heating some initial densification is observed at low temperature, possibly due to rearrangement of the particles under pressure associated with drying of the particle surfaces. A clear increase in the densification is observed already at very low temperatures (approximately from 400 °C to 800 °C for $U_{0.85}Th_{0.15}O_2$ and from 600 °C to 1000 °C for $U_{0.50}Th_{0.50}O_2$). This first stage is possibly associated with particle rearrangement [23] and densification due to creep through grain boundary sliding [24] and sintering of the small crystallites with a size of few nanometres. These findings are consistent with the crystallite growth curves (Fig. 4), in which it is seen that the diffusional processes in $U_{0.85}Th_{0.15}O_2$ nanopowder are active at lower temperatures compared to $U_{0.50}Th_{0.50}O_2$. At higher temperature the densification continues, however in the case for $U_{0.85}Th_{0.15}O_2$ the slope of the curve (Fig. 5) changes slightly which could indicate a different pathway.

Both powder compositions reach a relative density above 0.9 in constant rate sintering experiment (200 °C/min). The small decrease in density above 1600 °C could be explained as a sign of solarisation, or as an artefact introduced by the necessary correction for thermal expansion. The micrograph in Fig. 6 does not show indications of desintering and no further change in density was observed during the 2 min dwell at 1700 °C. Sintering in isothermal conditions at 1300 °C for only 2 min was sufficient to produce disks with relative density higher than 0.95 measured with the Archimedes' method (Table 1).

The diffraction pattern of the pellets sintered at 1700 °C confirmed a single phase and thus full solid solution, with a lattice parameter of 5.538(1) Å and 5.496(1) Å for $U_{0.50}Th_{0.50}O_2$ and $U_{0.85}Th_{0.15}O_2$, respectively.

The microstructures of the sintered pellets have been analysed by SEM (Fig. 6). The samples show in general a dense
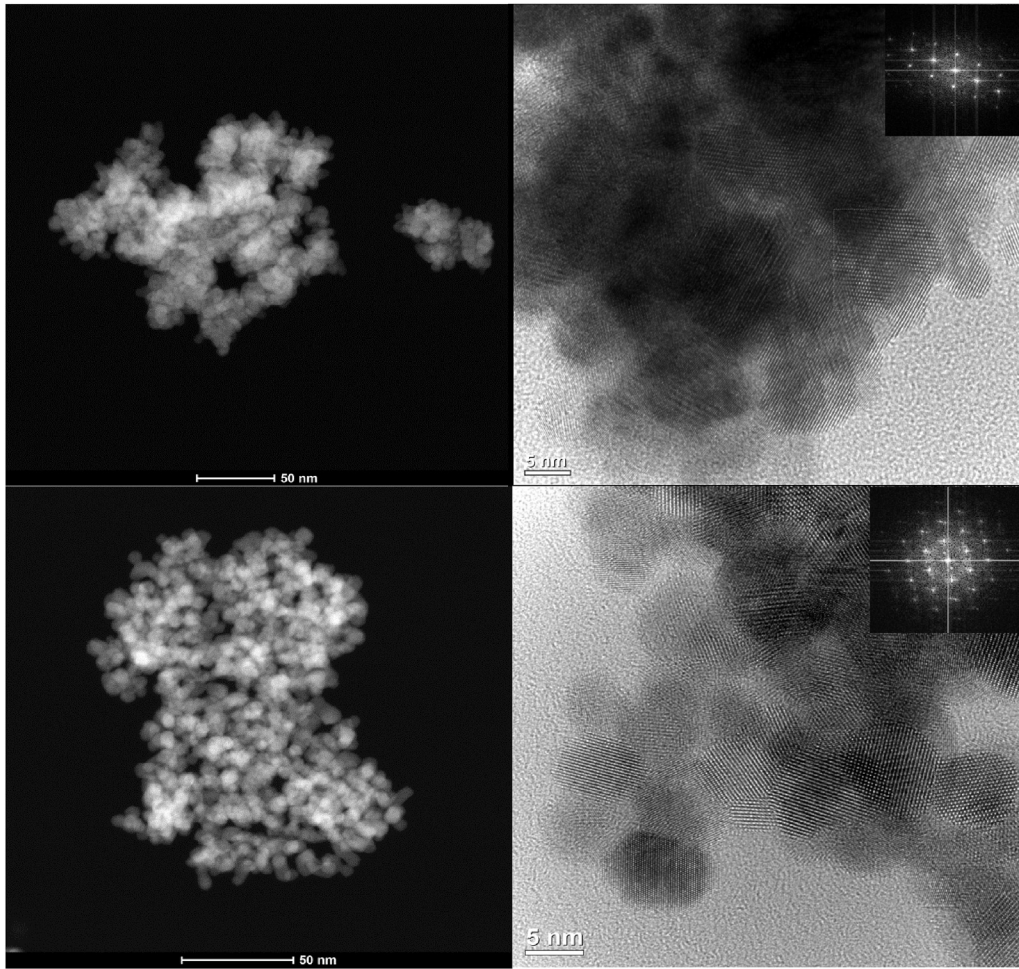
Fig. 3. STEM overview images and HRTEM micrographs (with FFT of an individual nanocrystal as inset) of nanocrystalline $U_{0.85}Th_{0.15}O_2$ (top) and $U_{0.50}Th_{0.50}O_2$ (bottom).
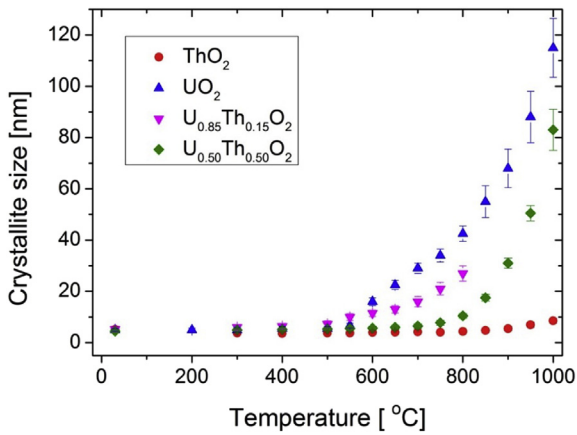

Fig. 4. The variation of the crystallite size of the $U_{1-x}Th_xO_2$ (x = 0; 0.15; 0.5; 1) as a function of temperature.
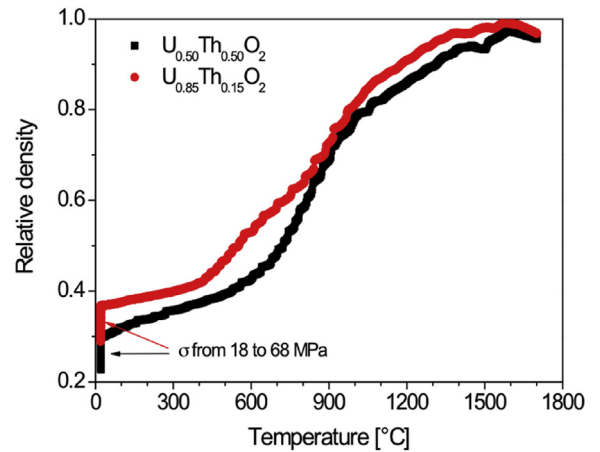

Fig. 5. Relative density as a function of the SPS temperature, with a heating rate of 200 °C/min and a constant pressure of 68 MPa. The first increase in density at room temperature is due to the pressure increase from 18 to 68 MPa.

microstructure. The average grain sizes are in 0.45−5.47 μm range and show a strong dependency with the sintering temperature (Table 1).

3.4. Nanoindentation

Nanoindentation has been performed in order to study the elastic modulus and hardness nanoindentation of the samples as a function of the composition and maximal sintering temperature (Table 1).

The elastic modulus (E) was found in all cases to be in the range of 265−275 GPa whereas the nanoindentation hardness (H_{IT}) was
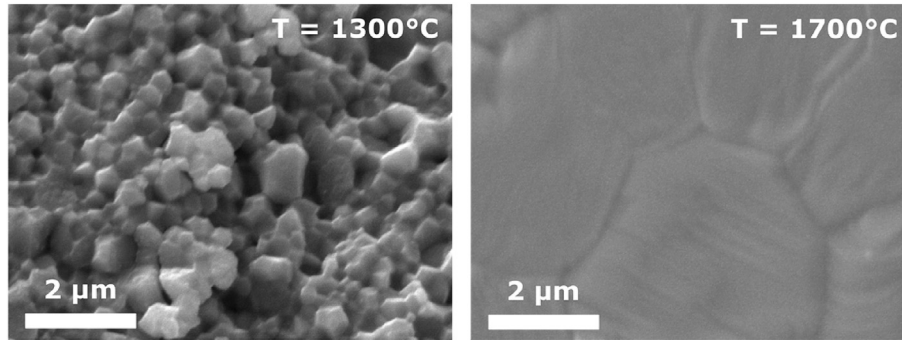
Fig. 6. SEM picture of the microstructures of $U_{0.85}Th_{0.15}O_2$ pellets sintered at a maximum temperature of 1300 °C (left, fracture surface) and 1700 °C (right, polished and thermally etched surface). The estimated grain sizes are 0.47(5) μm and 3.1(2) μm, respectively.

Table 1
Final relative density, grain size, elastic modulus and hardness of the sintered samples as a function of the composition and maximal sintering temperature.

Composition	T_{max} [°C]	ρ	Grain size [μm]	E [GPa]	H [GPa]
$U_{0.50}Th_{0.50}O_2$	1300	0.955	0.45(5)	[a]272(9)	[a]13.1(4)
$U_{0.50}Th_{0.50}O_2$	1700	0.957	5.5(3)	270(3)	11.2(3)
$U_{0.85}Th_{0.15}O_2$	1300	0.960	0.47(6)	266(6)	11.3(3)
$U_{0.85}Th_{0.15}O_2$	1540	0.958	1.20(6)	262(7)	11.2(1)
$U_{0.85}Th_{0.15}O_2$	1700	0.976	3.1(2)	275(5)	11.3(2)

[a] Pile-up observed.

in the range 11.2–11.3 GPa, with the exception of one single case: for $U_{0.50}Th_{0.50}O_2$ sintered at 1300 °C and grain size of 0.45 μm, a hardness of 13.1 GPa was derived. In this case, however, a consistent pile-up around the indent is observed (Fig. 7) which results in an overestimation of both elastic modulus and indentation hardness values, as the pile-up is not taken into account by the Oliver-Pharr analysis.

The grain size is known to be one of the variables affecting the hardness of materials. In ceramics, the relationship can be quite variable, going from an inverse dependency of the hardness with the grain size (Hall-Petch relationship) to a direct dependency [25]. In the present case the data are too limited to draw any conclusions, and the observed pile-up complicates the analysis. The measurements on $U_{0.85}Th_{0.15}O_2$ suggest an absence of a grain size effect on the hardness in the interval from 0.47 to 3.10 μm.

The comparison of the hardness and elastic modulus from nanoindentation tests with the values reported in the literature is not straightforward, as to the best of our knowledge no nanoindentation data on compounds with similar compositions are available. Muta et al. [2] measured elastic modulus and hardness by ultrasound methods and Vickers indentation; the values measured

here by nanoindentation are higher by approximately 10% and 50%, respectively. It is worth noting that the deformation mechanisms involved in nanoindentation may differ from those occurring in tests performed at larger scale such as ultrasounds, Vickers indentation and full-size tensile or bending tests [26]. In the case of nanoindentation the volume of sample probed by the indenter is extremely small. A typical indentation imprint in our samples is approximately 3–5 μm across with an average maximum penetration depth below 1 μm.

The higher hardness values measured with nanoindentation can be explained by the well documented Indentation Size Effect (ISE) [27]. ISE can be described as an increase in hardness with decreasing penetration depth (for geometrically self-similar indenters such as the Berkovich geometry). Different theories for this phenomenon have been proposed and research is still ongoing. A number of different explanations for ISE observed in ceramics involve mechanism associated with cracking, phase transformation and plastic deformation not driven by dislocation dynamics [28,29].

4. Summary and conclusions

We presented here for the first time the synthesis of single phase nanocrystalline $U_{1-x}Th_xO_2$ ($x = 0$ to 1) full solid solution through the hydrothermal decomposition of the oxalates under hot compressed water. For the applied reaction conditions, the crystallite size of the $U_{1-x}Th_xO_2$ solid solutions is constant around 5.5–6 nm, independent of the chemical composition. Remarkably, there is no observable size effect on the lattice parameters in $U_{1-x}Th_xO_2$ MOX nanoparticles for $x \geq 0.5$, at least down to a size of about 6 nm. Moreover, we have observed a stabilising effect of thorium for the 4 + oxidation state of uranium for the same compositional range.
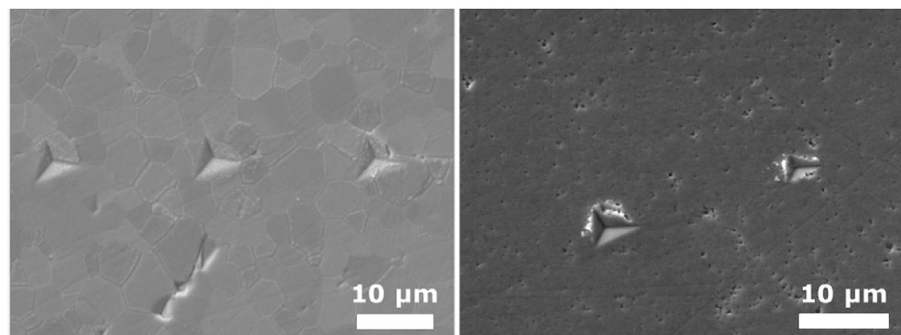

Fig. 7. Examples of indentation imprints showing absence of pile-up (left, $U_{0.50}Th_{0.50}O_2$ sintered at 1700 °C) and considerable pile-up (right, $U_{0.50}Th_{0.50}O_2$ sintered at 1300 °C).

Powders with compositions of $U_{0.85}Th_{0.15}O_2$ and $U_{0.50}Th_{0.50}O_2$ were consolidated in SPS, at temperatures as low as 1300 °C. The variation of the maximum sintering temperature in the 1300 °C-1700 °C range allowed the tailoring of the grain size in the 0.4—5.5 μm range. The measurement suggest an absence of a grain size effect on the nanoindentation hardness in the grain size interval and composition considered, although more data should be collected to confirm this observation.

Acknowledgements

References

[1] M.B. Schaffer, Abundant thorium as an alternative nuclear fuel. Important waste disposal and weapon proliferation advantages, Energy Policy 60 (2013) 4—12.

[2] H. Muta, Y. Murakami, M. Uno, K. Kurosaki, S. Yamanaka, Thermophysical properties of $Th_{1-x}U_xO_2$ pellets prepared by spark plasma sintering technique, J. Nucl. Sci. Technol. 50 (2013) 181—187.

[3] K.I. Björk, Thorium Fuels for Light Water Reactors, PhD Thesis, Chalmers University of Technology, Goteborg, 2015.

[4] IAEA TECDOC 1450, Thorium Fuel Cycle - Potential Benefits and Challenges, 2005.

[5] M. Teague, B. Gorman, J. King, D. Porter, S. Hayes, Microstructural characterization of high burn-up mixed oxide fast reactor fuel, J. Nucl. Mater. 441 (2013) 267—273.

[6] Q. Wang, G.-D. Li, S. Xu, J.-X. Li, J.-S. Chen, Synthesis of uranium oxide nanoparticles and their catalytic performance for benzyl alcohol conversion to benzaldehyde, J. Mater. Chem. 18 (2008) 1146—1152.

[7] R.M. Orr, H.E. Sims, R.J. Taylor, A review of plutonium oxalate decomposition reactions and effects of decomposition temperature on the surface area of the plutonium dioxide product, J. Nucl. Mater. 465 (2015) 756—773.

[8] N. Clavier, G.I. Nkou Bouala, J. Léchelle, J. Martinez, N. Dacheux, R. Podor, Novel approaches for the in situ study of the sintering of nuclear oxide fuel materials and their surrogates, Radiochim. Acta (2017) in press.

[9] V. Tyrpekl, J.-F. Vigier, D. Manara, T. Wiss, O. Dieste Blanco, J. Somers, Low temperature decomposition of U(IV) and Th(IV) oxalates to nanograined oxide powders, J. Nucl. Mater. 460 (2015) 200—208.

[10] V. Tyrpekl, M. Cologna, A. Cambriani, W. De Weerd, J. Somers, Preparation of bulk-nanostructured UO_2 pellets using high-pressure spark plasma sintering for LWR fuel safety assessment, J. Am. Ceram. Soc. 100 (2017) 1269—1274.

[11] O. Walter, K. Popa, O. Dieste Blanco, Hydrothermal decomposition of actinide(IV) oxalates: a new aqueous route towards reactive actinide oxide nanocrystals, Open Chem. 14 (2016) 170—174.

[12] C. Carrigan, R. Taylor, M. Sarsfield, $U_xTh_{1-x}(C_2O_4)_2$ solid characterization studies, Procedia Chem. 21 (2016) 349—356.

[13] N. Clavier, N. Hingant, M. Rivenet, S. Obbade, N. Dacheux, N. Barré, F. Abraham, X-ray diffraction and μ-Raman investigation of the monoclinic-orthorhombic phase transition in the $Th_{1-x}U_x(C_2O_4)_2 \cdot 2H_2O$ solid solutions, Inorg. Chem. 49 (2010) 1921—1931.

[14] V. Tyrpekl, C. Berkmann, M. Holzhäuser, F. Köpp, M. Cologna, T. Wangle, J. Somers, Implementation of a spark plasma sintering facility in a hermetic glovebox for compaction of toxic, radiotoxic, and air sensitive materials, Rev. Sci. Instrum. 86 (2015) 023904.

[15] W.C. Oliver, G.M. Pharr, An improved techniques for determining hardness and elastic modulus using load and displacement sensing experiments, J. Mater. Res. 7 (1992) 1564—1583.

[16] W. Trzebiatowski, P.W. Selwood, Magnetic susceptibilities of urania-thoria solid solutions, J. Amer. Ceram. Soc. 72 (1950) 4504—4506.

[17] S. Anthonysamy, G. Panneerselvam, S. Bera, S.V. Narasimhan, P.R. Vasudeva Rao, Studies on thermal expansion and XPS of urania-thoria solid solutions, J. Nucl. Mater. 281 (2000) 15—21.

[18] S. Hubert, J. Purans, G. Heisbourg, P. Moisy, N. Dacheux, Local structure of actinide dioxide solid solutions $Th_{1-x}U_xO_2$ and $Th_{1-x}Pu_xO_2$, Inorg. Chem. 45 (2006) 3887—3894.

[19] P. Cakir, R. Eloirdi, F. Huber, R.J.M. Konings, T. Gouder, Thorium effect on the oxidation of uranium: photoelectron spectroscopy (XPS/UPS) and cyclic voltammetry (CV) investigation on $(U_{1-x}Th_x)O_2$ (x= 0 to 1) thin films, Appl. Surf. Sci. 393 (2017) 204—211.

[20] R.V. Krishnan, G. Panneerselvam, P. Manikandan, M.P. Antony, K. Nagarajan, Heat capacity and thermal expansion of uranium-gadolinium mixed oxides, J. Nucl. Radiochem. Sci. 10 (2009) 19—26.

[21] P.S. Ghosh, P.S. Somayajulu, K. Krishnan, N. Pathak, A. Arya, G.K. Dey, Thermal expansion and thermal conductivity of (Th,U)O2 mixed oxides: a molecular dynamics and experimental study, J. Alloys Compd. 650 (2015) 165—177.

[22] L. Claparede, N. Clavier, N. Dacheux, A. Mesbah, J. Martinez, S. Szenknect, P. Moisy, Multiparametric dissolution of thorium-cerium solid solutions, Inorg. Chem. 50 (2011) 11702—11714.

[23] G.I. Nkou Bouala, N. Clavier, J. Léchelle, J. Monnier, C. Ricolleau, N. Dacheux, R. Podor, High-temperature electron microscopy study of ThO_2 microspheres sintering, J. Eur. Ceram. Soc. 37 (2017) 727—738.

[24] G. Antou, P. Guyot, N. Pradeilles, M. Vandenhende, A. Maître, Identification of densification mechanisms of pressure-assisted sintering, J. Mater. Sci. 50 (2015) 2327—2336.

[25] R.W. Rice, C.C. Wu, F. Boichelt, Hardness-grain size relations in ceramics, J. Am. Ceram. Soc. 77 (1994) 2539—2553.

[26] H. Gao, Y. Huang, Geometrically necessary dislocation and size-dependent plasticity, Scr. Mater. 48 (2003) 113—118.

[27] G.M. Pharr, E.G. Herbert, Y. Gao, The indentation size effect: A critical examination of experimental observations and mechanistic interpretations, Annu. Rev. Mater. Res. 40 (2010) 271—292.

[28] S.J. Bull, T.F. Page, E.H. Yoffe, An explanation of the indentation size effect in ceramics, Philos. Mag. Lett. 59 (1989) 281—288.

[29] A.J. Bushby, D.J. Dunstan, Plasticity size effects in nanoindentation, J. Mater. Res. 19 (2004) 137—142.